Refractive Effects, Turbulence, and the EOSTAR model

Stephen Doss-Hammel[a], Dimitri Tsintikidis[a],
Alexander van Eijk[b], and Gerard Kunz[b]

[a]Atmospheric Propagation Branch code 2858,
Space and Naval Warfare Systems Center, San Diego CA
[b] TNO Physics and Electronics Laboratory, The Hague, The Netherlands

ABSTRACT

An infrared signal or a laser beam propagating along a horizontal near-surface path will encounter substantial perturbations. The fluxes of momentum and heat near the surface are relatively large, and these in turn cause large changes in the propagated intensity, direction, and coherence. It is important to be able to accurately model the separate effects that generate changes in a propagated beam, and it is also important to combine the different factors accurately. We will present some evidence from field experiments to demonstrate how refractivity changes on a ten-minute scale are manifested in a recorded infrared transmission signal.

The *EOSTAR* (Electro-Optical Signal Transmission and Ranging) model is used to provide performance predictions for the experimental work. The *EOSTAR* model is built upon a geometrical optics approach to infrared propagation: a ray is traced through the propagation environment, and path-dependent perturbations to the signal can be determined. The primary computational tool for analysis of refractive effects in the *EOSTAR* model is a geometrical optics module that produces a ray-trace calculation for a given refractive environment. Based on the vertical profiles of temperature, humidity, refractive index structure parameter, and the calculated ray trajectories, *EOSTAR* calculates the path-integrated and spectrally-resolved transmission, background-radiation and path-radiation, as well as the scintillation and blur for a point source at any range and height position.

Keywords: ray-trace, geometrical optics, atmospheric refraction, mirages, propagation models, EOSTAR

1. INTRODUCTION

There are numerous systems either planned or proposed which are founded upon electromagnetic propagation over a long, near-surface path. These systems include point-to-point communications, surveillance, tracking, and directed energy weapons systems. Such systems require a capability to predict the electromagnetic propagation environment, and they often require a propagation path that passes at some points within a few meters of the water or land surface.

Propagation modeling in the near-surface environment can be a difficult problem since extended horizontal propagation paths in the atmospheric surface layer encounter relatively dynamic refractivity conditions. In this paper we discuss models for infrared and visible propagation, and we will describe the application of a geometrical optics model to analyze the near-surface atmospheric propagation environment.

2. MODELS FOR REFRACTIVE PROPAGATION

EOSTAR is a computational tool for the analysis of near-surface propagation effects. The *EOSTAR* model is based upon a geometrical optics tool that determines a ray-trace calculation for a given refractive environment.[1] The ray-trace data is then utilized to generate detailed information about geometrical transformations induced by the propagation environment.

Further author information: (Send correspondence to S.D.-H.)
S.D.-H.: E-mail: stephen.doss-hammel@navy.mil, Telephone: 619 553 4578

Infrared Technology and Applications XXX, edited by Bjørn F. Andresen,
Gabor F. Fulop, Proc. of SPIE Vol. 5406 (SPIE, Bellingham, WA, 2004)
0277-786X/04/$15 · doi: 10.1117/12.546625

Any geometrical optics ray-trace method must be initialized by a definition of the local refractivity field. We are interested in propagation over water and over land, and for most of the analysis we shall assume that, within the atmospheric surface layer, this field can be considered to be horizontally homogeneous. For optical and infrared frequencies, the primary determinant of the refractivity profile is the vertical temperature profile.

2.1. The Refractivity Gradient and Ray Curvature

The optical path calculation for a ray propagating in the atmosphere requires a determination of the refractivity field. The near-surface atmosphere is assumed to be horizontally homogeneous. The vertical structure is divided into layers, and for each layer a refractivity gradient can be determined. We determine the refractivity gradient by means of a micro-meteorological bulk model; alternatively, the refractivity gradient can be found in terms of the vertical temperature gradient. Our method to determine ray trajectories is thus a variation on an approach described by Lehn[2] in which the vertical temperature gradient alone is required. Lehn's approach is described below.

A ray propagating through a medium with a gradient in refractive index will define a curved path. The refractive index n is found :

$$n = 1 + \alpha(\lambda)\frac{P}{T},$$

where $\alpha(\lambda) = (77.6 + 0.584\lambda^{-2}) \times 10^{-6}$ and λ is the wavelength in micrometers. Hence the refractive gradient is:

$$\frac{dn}{dz} = \frac{\alpha(\lambda)}{T^2}\left(T\frac{dP}{dz} - P\frac{dT}{dz}\right) \tag{1}$$

Using the hydrostatic equation with density ρ and gravitational acceleration g, and $\beta = 3.485 \times 10^{-3}$, we get

$$\frac{dn}{dz} = -\frac{\alpha(\lambda)P}{T^2}\left(g\beta + \frac{dT}{dz}\right) \tag{2}$$

The curvature κ of a ray is defined such that positive curvature means a ray is concave towards the earth:

$$\kappa = -\frac{\sin(\zeta)}{n}\frac{dn}{dz}. \tag{3}$$

where ζ is the angle between the ray and the normal to the local surface tangent plane. The radius of curvature r is $r = 1/\kappa$, and this yields

$$r = \frac{nT^2}{\sin(\zeta)\alpha(\lambda)\ P\ (g\beta + dT/dz)} \tag{4}$$

where $r > 0$ defines a ray that is concave down toward the earth.

For a ray-trace calculation the atmosphere is divided into concentric shells of constant thickness and constant height. Within each shell or layer, a refractivity gradient is defined as a function of the temperature gradient. We take the temperature gradient within the layer to be constant as well, and therefore the radius of curvature for each layer is a constant.

The local coordinate system is further transformed to bring the curved surface of mean sea level to a horizontal plane (a "flat earth" representation). Thus the x-axis in the two dimensional representation is the mean sea surface, and range information along the propagation path is measured in this coordinate. The z-axis represents the vertical offset from $z = 0$ at mean sea level. A characteristic radius of curvature is then assigned to each layer using eqn. (4) above.

3. FIELD MEASUREMENTS AT CHINA LAKE CALIFORNIA

The effects of a changing refractive field can be seen in a most pronounced way in imaging data obtained for propagation paths over land. In this section we will consider data from a one-hour period at sunrise. The data were taken at the Naval Air Warfare Center (NAWC) China Lake, California in November and December of 1999. Transmission measurements were made with a mid-wave detector (3.6μm – 4.1μm) and a long-wave (9.8μm – 11.3μm) detector. The measurements in the mid-wave IR showed some unusual effects, including periods of transmission which exceeded the free-space intensity by nearly 500%.

Associated with the increase in received power is a change in the apparent vertical extent and position of a source or target. We collected intermittent video imagery alongside the transmissometer receiver, and several of these images are shown below. These images were recorded from a small CCD camera coupled to a Questar telescope, with a resultant field of view of ≈ 5.8 milliradian. A composite image comprising five thin slices from five different recording periods is shown in fig. 1. At the left end of the figure is shown a slice from a sequence recorded at 8:41 UT (which is 12:41 a.m. PST); only the source can be seen. Note that the source is nearly at the top of the frame at this time of day. The next four slices show in succession the images from 15:03, 15:23, 15:43, and 16:23 (all UT). In each of these four slices, the source is at the right edge of the prominent bright white blurry object (a tracking radar and associated small building).

4. EOSTAR SIMULATION OF REFRACTIVE DISTORTIONS

With the EOSTAR model it is possible to simulate the effects of a change in the meteorological conditions. In this section we will show how the model can generate results that preserve the essential elements of the changes suggested by the imagery displayed in fig. 1. The nature of the refractive field over the propagation path can actually be calculated in some detail if the local topographic changes are incorporated in the ray-trace model. In this paper, we will simply look at the results of computations for a path defined over a flat planar surface.

4.1. The Vertical Temperature Profile

There are two primary methods for the definition of a vertical temperature profile within the *EOSTAR* model. A first method utilizes a micro-meteorology approach, and the generation of a continuous vertical temperature profile is based upon a surface layer similarity theory developed by Monin and Obukhov. This approach is widely used, and has been described elsewhere.[3–7] The input data for this approach consist of measurements of temperature, pressure, humidity, and wind-speed at some fixed point within the surface layer, and a surface temperature and relative humidity measurement. There are currently three possible micro-meteorological models available[3–5] that can be combined with either of two stability functions to generate a vertical temperature profile.

A second option is to measure the vertical profile data accurately at multiple levels. These values can then be inserted directly into the model to define a piecewise linear approximation of the vertical profile. This data is then used to determine the vertical refractivity field. In this paper we will utilize this second option. For the duration of the test at China Lake, a 30-meter meteorological tower was installed at the mid-point of the 11.25 km propagation path. The surface temperature was measured, and temperature and humidity were measured at heights of 1 m, 3 m, 10 m, 20 m, and 30 m. Wind-speed and direction was measured at 3 m, 10 m, and 30 m, and pressure was measured at the surface and at 10 m. Each of these measurements was made and recorded every 10 minutes.

4.2. Imagery simulation

We will present a sequence of ray-trace calculations for the set of observations presented in fig. 1. It is important to re-iterate that the calculations shown here are intended to be a blend of quantitative and qualitative information. In order for an accurate solution, the details of the surface topography must be included in the ray-trace analysis. However the first-order effects can be seen even in the simulations using just a flat surface topography.

The camera module in EOSTAR allows control of most aspects of an imaging system, and in our case the 5.8 milliradian field of view and a height of 5 m is used to position the camera. In fig. 2 we show a ray-trace

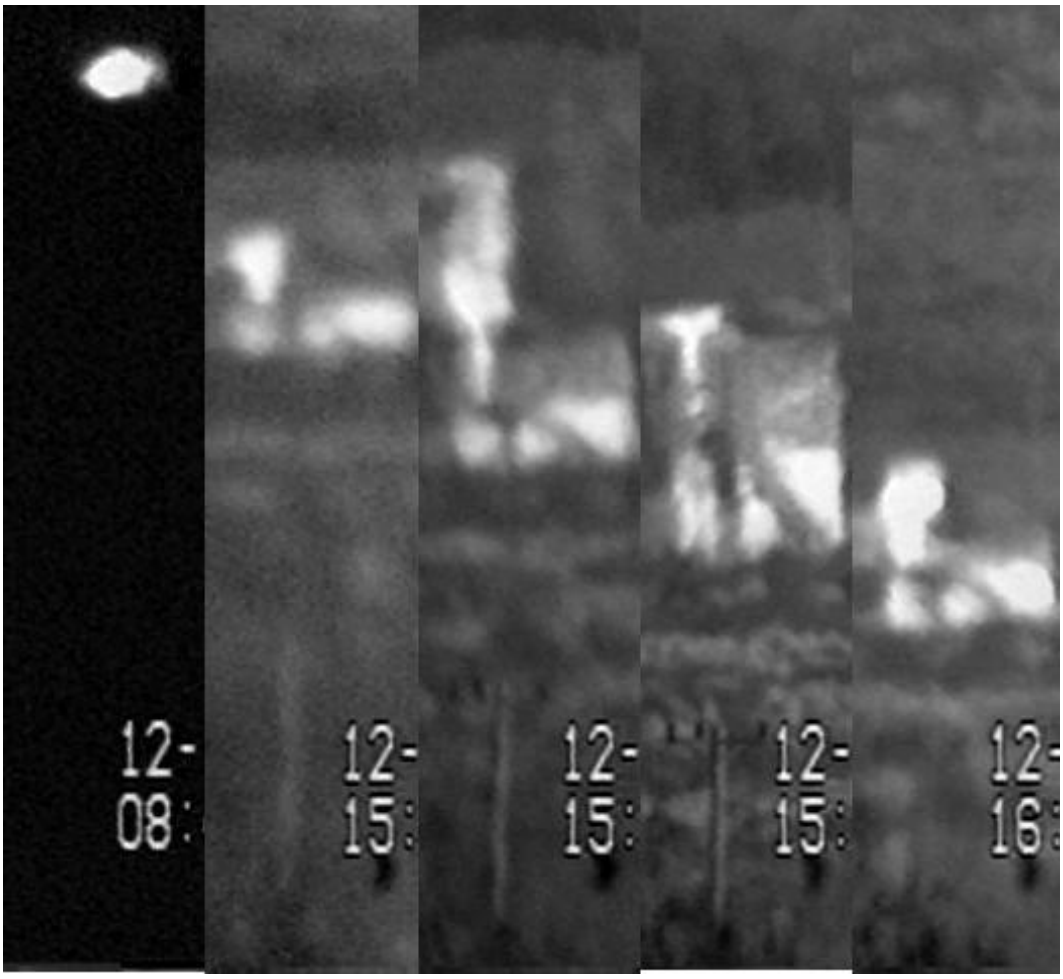

Figure 1. A composite of images from five different data sequences. The blurry white object is a tracking radar and a small building, and the source is at the right edge of the object. From the left, images were recorded at 8:41, 15:03, 15:23, 15:43, and 16:23 UT, which is 12:41 a.m., 7:03 a.m., 7:23 a.m., 7:43 a.m. and 8:23 a.m. PST. Note the pronounced change in elevation over the 8-hour period.

for the 'atmosphere-free' conditions, and the resulting image. A target pole consisting of a thick vertical blue line segment at the range of 11.25 km indicates the range and height of the extended target (in this case, 30 m high). The image that results from the transformation induced by the vertical refractivity gradient uses the target pole as the source object. The topological nature of the resultant image can be highly non-uniform over the vertical extent of the target: some points of the target object may not appear in the image at all, while other points in the target object can appear at several disconnected points in the image.

The *EOSTAR* model has been developed primarily as a model for maritime atmospheric surface layer propagation analysis, and thus we have used a ship as our standard extended target to illustrate the distortions induced by the refractive field. The variations and complexity of the ship help to visually demonstrate the non-uniformity of the distortions that can occur in the image. What should be noted in the figure is the relative elevation of the horizon, and the shape and extent of the ship image.

The second characteristic that we intend to follow is the intensity and elevation of a point source in the object plane. A point source is defined at an elevation of 11.9 m and a range of 11.25 km. This source is visible as a combined cross-hair and red diamond on the target pole at the range of 11.25 km. The geometric amplification factor (or refractive propagation factor) is height dependent, and we will follow the amplification

at this point through the series of changing refractive field conditions.

The effect of the change in the refractive field can be seen in the sequence of figs. 3, 4, 5, 6, and 8 which cover the period from 15:03 to 16:03 UT, or 7:03 to 8:03 PST. We reiterate that the mechanism behind the changes in refractive field is the change in meteorological conditions. The most significant component of the changing meteorological conditions is the change in vertical temperature profile, and in particular the change in the first three meters above the surface.

In fig. 3, the horizon is greatly elevated above the geometric level seen in fig. 2. In fact, the horizon is elevated nearly 3 milliradians above the 'atmosphere-free' state, and the target point is elevated from $\phi_{\text{refract}} = -0.33$ mrad to $\phi_{\text{refract}} = 1.83$ mrad.

We also calculate a quantity called the geometric amplification: the total of the geometric amplification for a given target yields a refractive propagation factor F^2. This factor describes the increase or decrease in signal intensity due to geometric factors alone, and it will be discussed in more detail below. The neutral, 'atmosphere-free' case has a factor $F^2 \equiv 1$. In fig. 3 the calculated propagation factor for the point target is found to be $F^2 = 0.13$. This signal diminution can be noted visually by the great compression of the lower hull portion of the ship image. It is important to note that the propagation factor is by no means a constant over the height of any extended target; it is a strong function of elevation.

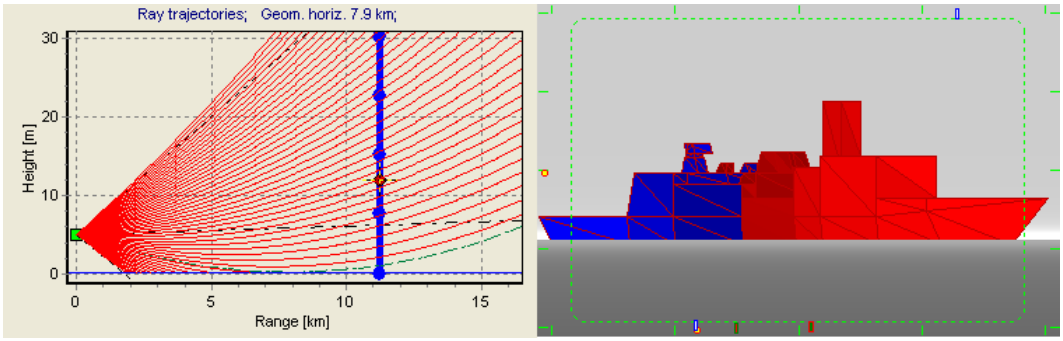

Figure 2. The left-side panel shows the ray-trace for a camera height of 5 m. The vertical thick blue 'pole' at 11.25 km represents a target of 30 m overall height. The cross-hair shown on the target pole at 11.9 m height is the point at which the elevation angle and the propagation factor is measured. In 'atmosphere-free' conditions, the target point is at an elevation angle $\phi_{\text{refract}} = -0.33$ mrad, and the propagation factor $F^2 = 1.0$.

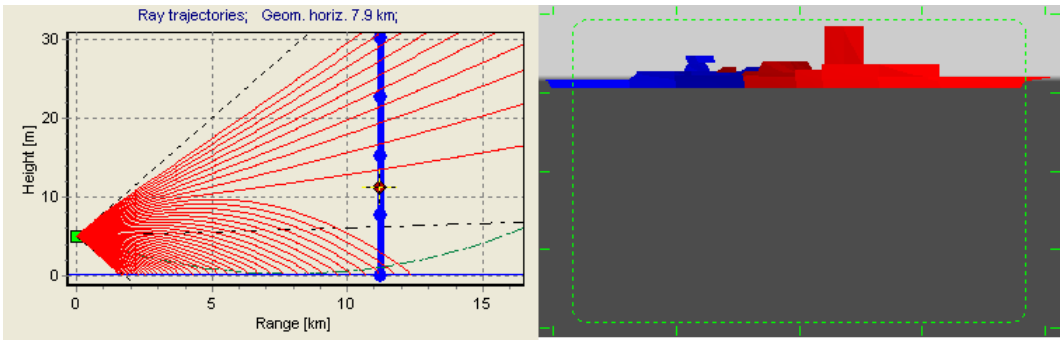

Figure 3. At 15:03 UT, the target point is at an elevation angle $\phi_{\text{refract}} = 1.83$ mrad, and the propagation factor $F^2 = 0.13$. The lower portion of the ship's hull is greatly compressed, corroborating the propagation factor assessment.

Twenty minutes later, (at 15:23 UT) as shown in fig. 4, the target point is at an elevation angle $\phi_{\text{refract}} = 1.48$ mrad, and the propagation factor $F^2 = 0.27$. We do not show the temperature profile corresponding to each ray-trace, but at this time of day (15:23 UT=7:23 PST) the sun is rising and the earth's surface is beginning

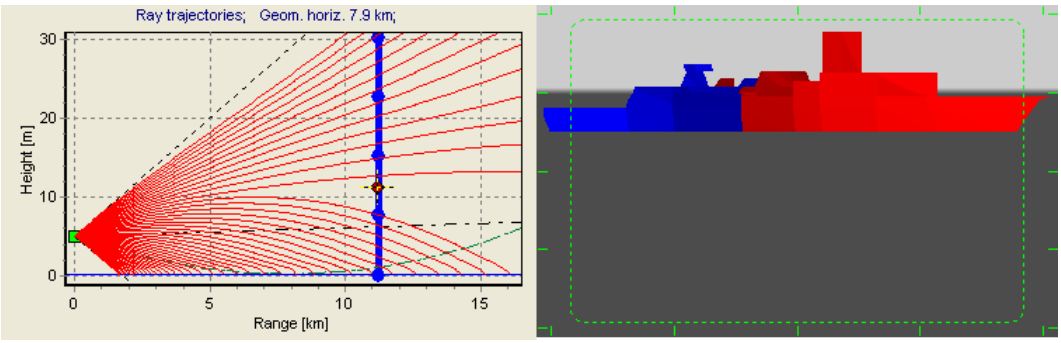

Figure 4. At 15:23 UT, the target point is at an elevation angle $\phi_{\text{refract}} = 1.48$ mrad, and the propagation factor $F^2 = 0.27$.

to warm. This is modifying the lowest portion of the temperature profile, and hence the lowest part of the ray-trace. After 10 minutes, at 15:33 UT, the surface has warmed sufficiently to create a near-surface sub-refractive mirage (see fig. 5). This can be seen clearly in the ship image at the bow: the characteristic slant of the bow terminates at the mirage fold-line and begins to slope in the opposite direction.

At 15:43, (fig. 6) the mirage distortion has become even more pronounced, and the apparent horizon has descended further. The point source elevation is $\phi_{\text{refract}} = 0.17$ mrad, and the propagation factor $F^2 = 1.61$. This means that the point source signal is now being amplified above the free-space value (161% of the free-space value).

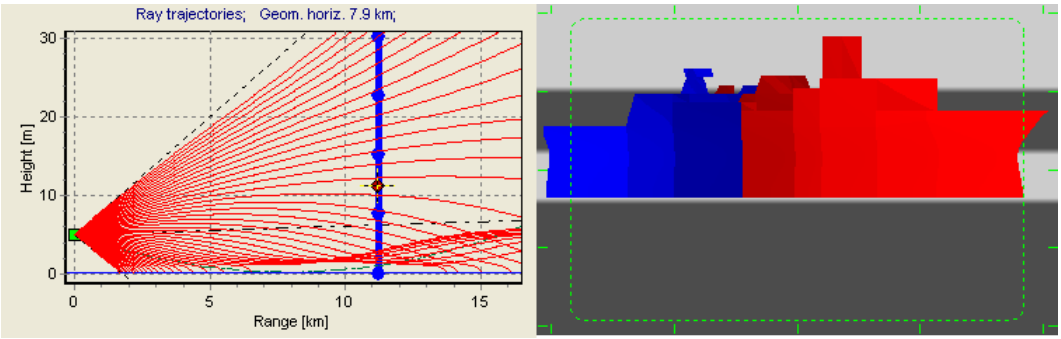

Figure 5. At 15:33 UT, the target point is at an elevation angle $\phi_{\text{refract}} = 1.24$ mrad, and the propagation factor $F^2 = 0.61$. Note the sub-refractive mirage causing a second inverted image of the lower portion of the ship's hull. Also note the strip of sky topped by a second strip of sea surface.

A similar ray-trace corresponding to a sub-refractive mirage is apparent at 15:53 UT, as seen in fig. 7. Although it is not apparent in the figure, the mirage image does not include the point target probe, and the amplification from the propagation factor $F^2 = 1.18$ is due to a single ray-path. However, at 16:03 UT, (fig. 8) there are two separate ray paths to the point target. For the first path, $\phi_{\text{refract}}(1) = -1.26$ mrad and for the second path, $\phi_{\text{refract}}(2) = -0.54$ mrad. The refractive propagation factor is $F^2 = 4.23 + 1.07 = 5.3$, determined by summing the geometric amplifications over all possible ray-paths.

5. THE TRANSFER MAP

The amplitude and elevation observations highlighted in the previous section are displayed quantitatively only for a single target point. Furthermore, it is difficult to decipher both the orientation and the magnification in mirage images. A superior method to accurately calculate the propagation effects on images is to determine the transfer map for the given refractive field. This map makes it possible to calculate both elevation offset and the

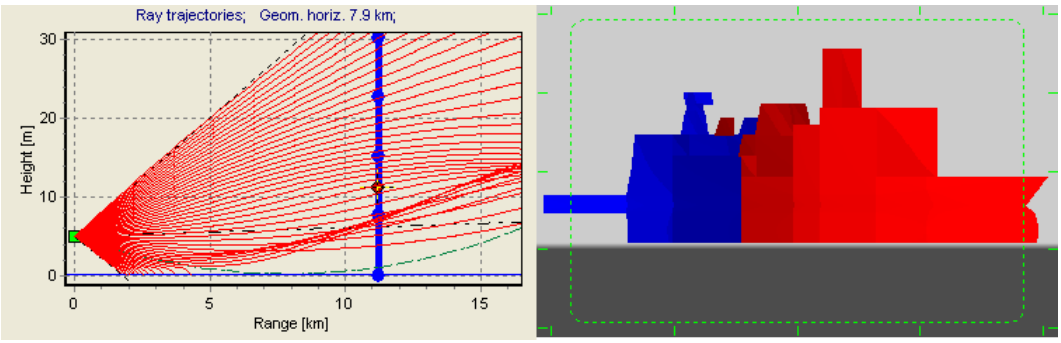

Figure 6. At 15:43 UT, the target point is at an elevation angle $\phi_{\text{refract}} = 0.17$ mrad, and the propagation factor $F^2 = 1.61$.

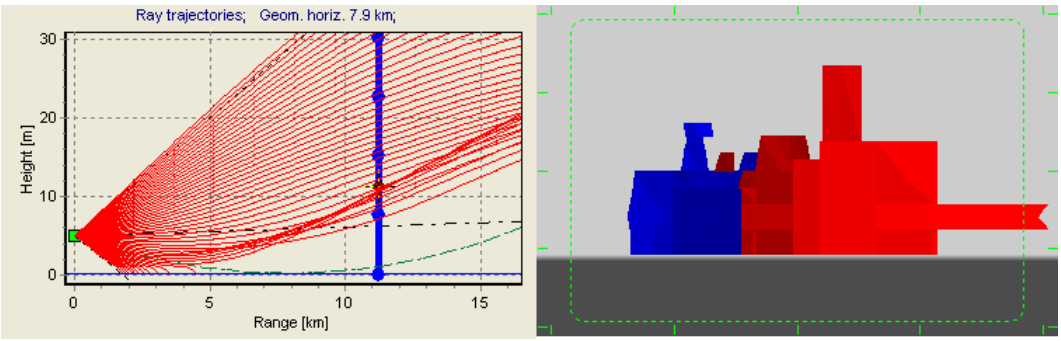

Figure 7. At 15:53 UT, the target point is at an elevation angle $\phi_{\text{refract}} = -0.42$ mrad, and the propagation factor $F^2 = 1.18$.

refractive propagation factor (or geometric gain) for an arbitrary height at a given range.[8] The calculation of a transfer map is done in the *EOSTAR* model, and two examples are shown in fig. 9.

The transfer map relationship is a map from the geometric 'atmosphere-free' angular position (ϕ_{geom}) to the refractive 'apparent' angular position (ϕ_{refract}). The transfer map is dependent upon the receiver height z_r at range $x = 0$, and it is defined for a vertical plane at the range point $x = x_t$. It is determined by finding all rays ρ_{refract} originating at the receiver location $(0, z_r)$ which intersect a vertical plane at range $x = x_t$. The transfer map defines the dependence of elevation angles at a selected range: $\phi_{\text{geom}}(\phi_{\text{refract}})$.

The two points of infinite derivative on this curve defining the transfer map in the right-hand plot of fig. 9

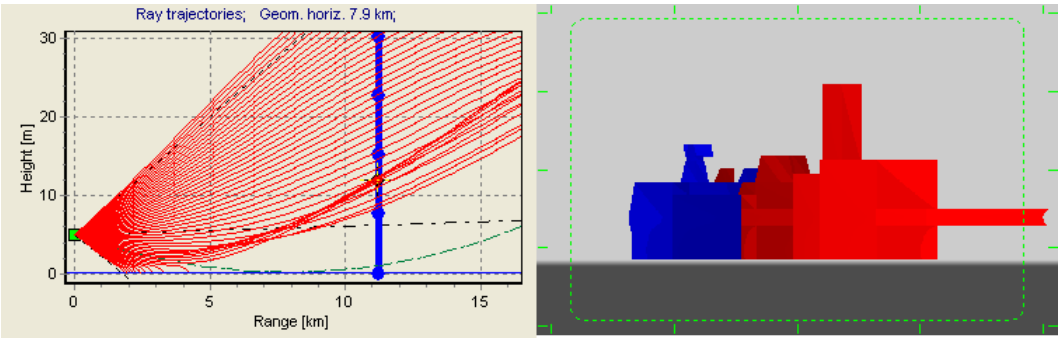

Figure 8. At 16:03 UT, the target point is seen as two distinct images, one at an elevation angle $\phi_{\text{refract}}(1) = -1.26$ mrad and the second at $\phi_{\text{refract}}(2) = -0.54$ mrad. The propagation factor $F^2 = 4.23 + 1.07 = 5.3$ is determined as the sum over all contributors.

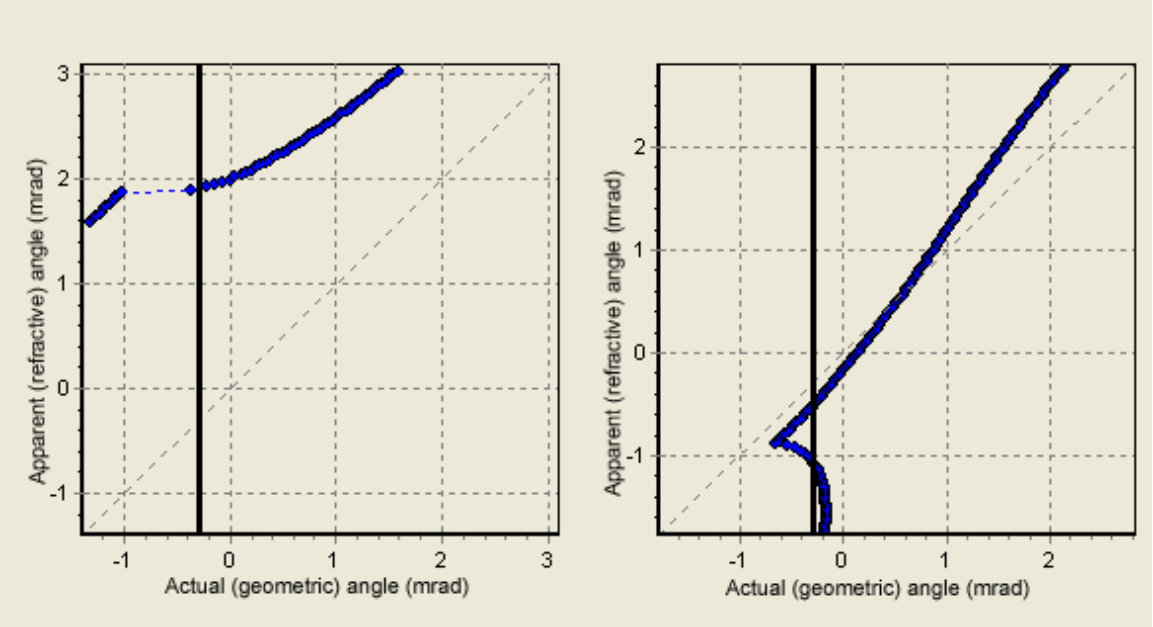

Figure 9. The transfer map is a transformation from the 'atmosphere-free' actual angular position ϕ_{geom} to the refractive apparent angular position ϕ_{refract}. The transfer map on the left is calculated for the ray-trace shown in fig. 3 at a range of 11.25 km. The dotted-line of $\phi_{\text{refract}} = \phi_{\text{geom}}$ indicates an identity transformation (the atmosphere-free case), and the vertical black line, which is positioned at an actual angular value $\phi_{\text{geom}} = -0.33$ mrad, indicates the point-target position. The map on the right depicts the transformation for the ray-trace shown in fig. 8. The vertical black line intersects the transfer function at two points, corresponding to the erect and inverted mirage images.

correspond to two caustic points in the ray-trace envelope. The apparent cusp in the transfer map is an artifact induced by the use of a piecewise linear approximation to the vertical temperature profile, which in turn induces a discontinuity in the vertical temperature gradient. The actual continuously varying profile will not exhibit such behavior.

There are three important elements that can be determined with the transfer map: 1) the apparent elevation of a given point source; 2) the existence and orientation (erect vs. inverted) of mirage images; 3) the local magnification or minification of the image at a given point. The magnification δ of the image is determined by

$$\delta = \left| \frac{d\phi_{\text{refract}}}{d\phi_{\text{geom}}} \right| \tag{5}$$

and the orientation of the image (erect or inverted) is given by the sign of $d\phi_{\text{refract}}/d\phi_{\text{geom}}$ with a positive sign corresponding to an erect image and a negative sign corresponding to an inverted image.

6. THE REFRACTIVE PROPAGATION FACTOR

We have discussed the use of the refractive propagation factor to describe the "geometric" gain, which is a change in signal intensity due entirely to the nature of the refractive field between target and sensor.[9] The term *refractive propagation factor* has been borrowed from radio-frequency propagation models. The word "refractive" is appended to indicate that changes in field amplitude due to refractive effects are included, but *not* changes due to any reflection of the propagating beam. The refractive propagation factor is a function of both the receiver location and the transmitter location.

The propagation factor F is defined as the ratio between the actual field amplitude at a selected field point and the corresponding field amplitude at that point in free-space propagation conditions. It can be determined by summing the geometric gain over all possible ray-paths between source and sensor.

The field intensity at the receiver is given in terms of the field amplitude propagation factor F by

$$F^2 = \sum_{\phi_{\text{refract}}} \left| \frac{d\phi_{\text{refract}}/dz}{d\phi_{\text{geom}}/dz} \right|_{(x,z)=(x_t,z_t)} \tag{6}$$

where the summation is over all values $-\pi/2 \leq \phi_{\text{refract}} \leq \pi/2$ for which rays terminate at (x_t, y_t). The propagation factor is defined for piecewise horizontally homogeneous environments, and it is dependent only on the spatial locations of the source point and receiver point in space. It is therefore necessary mathematically for the definition to include the full π-radian fan of rays for ϕ_{refract} to ensure that all rays from a source are accounted for at the receiver. Therefore at the upper and lower summation limits, $\phi_{\text{geom}} = \phi_{\text{refract}} = \pi/2$ and $\phi_{\text{geom}} = \phi_{\text{refract}} = -\pi/2$ since it is only the vertical rays that are certain to be undeviated in a piecewise horizontally homogeneous propagation environment. In practice, the field of view of a sensor will generally be considerably less than π radians.

We will compare the transfer maps for the two end-points of the sequence presented above, namely the transfer map at 15:03 UT (for the ray-trace in fig. 3) and the transfer map at 16:03 UT (for the ray-trace in fig. 8). These are shown in the left-side and right-side panels of fig. 9 respectively, and the discrete blue points represent a continuous curve. When the geometric, or atmosphere-free angular elevation is specified on the abscissa, the resultant image values at the camera are determined on the ordinate. In the example of fig. 9, the left-side panel shows an input abscissa value of $\phi_{\text{geom}} = -0.33$ mrad, for the environment of fig. 3 at 15:03 UT. The resultant output image elevation is $\phi_{\text{refract}} = 1.83$ mrad. The propagation factor calculation prescribed by eqn. (6) is $F^2 = |d\phi_{\text{refract}}/d\phi_{\text{geom}}| = 0.13$, indicating that geometric effects alone reduce the signal to 13% of its free-space intensity.

There can be multiple output ordinate values as in the case shown in the right-side panel of fig. 9 at 16:03 UT. The same input value $\phi_{\text{geom}} = -0.33$ mrad is mapped to two separated output points: $\phi_{\text{refract}}(1) = -1.26$ mrad, and $\phi_{\text{refract}}(2) = -0.54$ mrad. Note that $d\phi_{\text{refract}}(1)/d\phi_{\text{geom}} = -4.23$, and $d\phi_{\text{refract}}(2)/d\phi_{\text{geom}} = +1.07$ The propagation factor calculation of eqn. (6) can be demonstrated for this case: the propagation factor simply sums the magnitudes of the slopes of the transfer function at all points intersected by the vertical line indicating the geometric elevation of the object point.

$$F^2 = \left| \frac{d\phi_{\text{refract}}(1)}{d\phi_{\text{geom}}} \right| + \left| \frac{d\phi_{\text{refract}}(2)}{d\phi_{\text{geom}}} \right| = |-4.23| + |1.07| = 5.3 \tag{7}$$

This implies that the received signal will be $\approx 530\%$ of the free-space value in the absence of signal extinction factors. Although the evidence is not presented here, we did find mid-wave infrared transmission signal intensities that were 460% of the free-space value at 15:46 UT.

7. CONCLUSIONS

We have provided evidence of the dynamic and rapidly mutable nature of image propagation in the near-surface environment. During the course of a day, propagation conditions may change considerably, but we have shown that substantial changes also occur over ten-minute intervals. We have presented examples for propagation over land, for which these changes are larger and more dramatic. However, similar changes can occur over a reduced dynamic range for propagation paths over water, particularly for littoral regions. For long near-surface propagation paths, it is crucial to be able to model the various observed effects in order to optimize any signal transmission device, or to understand how best to manipulate the environmental conditions.

The *EOSTAR* model provides the requisite optical calculations by means of a geometric optics approach. *EOSTAR* is configured to provide accurate image distortion and 'visibility' predictions. The fact that the distortions are non-uniform in the vertical direction is a critical feature of the actual image distortions and the *EOSTAR* predictions. A precise determination of the type and intensity of the distortion, as a function of height, is available through the transfer map. The transfer map is a fundamental tool made possible by the creation of a ray-trace calculation. The transfer map enables the prediction of elevation changes and the appearance and orientation of mirages.

Another consequence of the transfer map calculation within the geometric optics approach is the capability to compute a geometric gain induced by the refractivity field. This refractive propagation factor is a necessary first-order component in a complete model for near-surface horizontal path infrared or optical transmission. The refractive effects are shown in the example to be substantial determinants of the received signal intensity. The refractive propagation factor is a multiplicative quantity derived entirely from the local refractivity field and the geometry of the complete propagation system.

We have presented examples of some of the first-order uses of the ray-trace techniques. There is also a second-order set of transmission calculations that is made possible by the ray method within *EOSTAR*. Both extinction and scintillation are height-dependent quantities in the atmospheric surface layer, and thus the effects on beam quality are also height-dependent. The determination of a ray-path provides an accurate framework for the calculation of strongly path-dependent beam degradation effects such as aerosol extinction, scintillation and the refractive index structure function. Each of these quantities is very important to the final determination of signal intensity or image quality.

REFERENCES

1. G.J. Kunz, M.M. Moerman, A.M.J. van Eijk, S.M. Doss-Hammel, and D. Tsintikidis, "EOSTAR: an electro-optical sensor performance model for predicting atmospheric refraction, turbulence, and transmission in the marine surface layer", in *Optics in Atmospheric Propagation and Adaptive Systems*, J. Gonglewski and K. Stein, ed., *Proc. SPIE* **5237**, pp. 81–92, 2003.
2. W. Lehn, *Appl. Math. Model.* **9,** 447, 1985.
3. S.D. Smith, "Coefficients for sea surface wind stress, heat flux, and wind profiles as a function of wind speed and temperature", J. Geophys. Res, **93**, pp. 15467–15472, 1988.
4. K.L. Davidson, G.E. Schacher, C.W. Fairall and A.K. Goroch, "Verification of the bulk method for calculating over water optical turbulence", *Appl. Opt.* 20, 17, pp. 498-502, 1981.
5. W.T. Liu, K. Katsaros and J. A. Businger, "Bulk parameterization of air-sea exchanges of heat and water vapor including the molecular constraints at the surface", *J. Atmos. Sci.* **36**, pp. 1722-1735, 1979.
6. G.J. Kunz, "ARTEAM, Advanced ray tracing with Earth atmospheric models", in *Targets and Backgrounds VII: Characterization and Representation*, W.R. Watkins, D. Clement and W.R. Reynolds, ed., *Proc. SPIE* **4718**, pp. 397–404, 1992.
7. S.P. Arya, *Introduction to Micrometeorology*, Academic Press, Inc., San Diego, 1988.
8. Doss-Hammel, S., "Mirages, Magnification, and the Refractive Propagation Factor", in *Infrared Technology and Applications*, B. Andresen, G. Fulop and M. Strojnik, ed., *Proc. SPIE* **4820**, pp. 840–848, 2002.
9. Doss-Hammel, S. M., Zeisse, C. R., Barrios, A. E., de Leeuw, G., Moerman, M., de Jong, A. N., Frederickson, P. A., Davidson, K. L., "Low-Altitude Infrared Propagation in a Coastal Zone: Refraction and Scattering", *Applied Optics* **41**, pp. 3706–3724, 2002.